

Site-Selective Real-Time Observation of Bimolecular Electron Transfer in a Photocatalytic System Using L-Edge X-Ray Absorption Spectroscopy**

Alexander Britz,^{*,[a, b, c]} Sergey I. Bokarev,^[d] Tadesse A. Assefa,^[a, c, i] Èva G. Bajnóczi,^[e] Zoltán Németh,^[e] György Vankó,^[e] Nils Rockstroh,^[f] Henrik Junge,^[f] Matthias Beller,^[f] Gilles Doumy,^[g] Anne Marie March,^[g] Stephen H. Southworth,^[g] Stefan Lochbrunner,^[d] Oliver Kühn,^[d] Christian Bressler,^[a, b, c] and Wojciech Gawelda^[a, h, j]

Time-resolved X-ray absorption spectroscopy has been utilized to monitor the bimolecular electron transfer in a photocatalytic water splitting system. This has been possible by uniting the local probe and element specific character of X-ray transitions with insights from high-level ab initio calculations. The specific target has been a heteroleptic $[\text{Ir}^{\text{III}}(\text{ppy})_2(\text{bpy})]^+$ photosensitizer, in combination with triethylamine as a sacrificial reductant and $\text{Fe}_3(\text{CO})_{12}$ as a water reduction catalyst. The relevant molecular

transitions have been characterized via high-resolution Ir L-edge X-ray absorption spectroscopy on the picosecond time scale and restricted active space self-consistent field calculations. The presented methods and results will enhance our understanding of functionally relevant bimolecular electron transfer reactions and thus will pave the road to rational optimization of photocatalytic performance.

[a] Dr. A. Britz, Dr. T. A. Assefa, Prof. Dr. C. Bressler, Prof. Dr. W. Gawelda
European XFEL, Holzkoppel 4, 22869 Schenefeld, Germany
E-mail: mail@alexbritz.de

wojciech.gawelda@amu.edu.pl

[b] Dr. A. Britz, Prof. Dr. C. Bressler
The Hamburg Centre for Ultrafast Imaging
Luruper Chaussee 149, 22761 Hamburg, Germany

[c] Dr. A. Britz, Dr. T. A. Assefa, Prof. Dr. C. Bressler
Department of Experimental Physics, Universität Hamburg
Jungiusstraße 9, 20355 Hamburg, Germany

[d] Dr. S. I. Bokarev, Prof. Dr. S. Lochbrunner, Prof. Dr. O. Kühn
Institut für Physik, Universität Rostock
Albert-Einstein-Str. 23–24, 18059 Rostock, Germany

[e] Dr. È. G. Bajnóczi, Dr. Z. Németh, Dr. G. Vankó
Wigner Research Centre for Physics
H-1525 Budapest, Hungary

[f] Dr. N. Rockstroh, Dr. H. Junge, Prof. Dr. Dr. h.c. mult. M. Beller
Leibniz-Institut für Katalyse
Albert-Einstein-Str. 29a, 18059 Rostock, Germany

[g] Dr. G. Doumy, Dr. A. M. March, Dr. S. H. Southworth
Chemical Sciences and Engineering Division
Argonne National Laboratory
9700 S. Cass Ave, 60439 Lemont, IL, USA

[h] Prof. Dr. W. Gawelda
Faculty of Physics, Adam Mickiewicz University
ul. Uniwersytetu Poznańskiego 2, Poznań, 61-614, Poland

[i] Dr. T. A. Assefa
Stanford Institute for Materials and Energy Sciences
SLAC National Accelerator Laboratory, Menlo Park, CA 94025, USA

[j] Prof. Dr. W. Gawelda
Department of Chemistry, Faculty of Sciences
Universidad Autónoma de Madrid and IMDEA-Nanoscience
Ciudad Universitaria de Cantoblanco, 28049 Madrid, Spain

[**] A previous version of this manuscript has been deposited on a preprint server (arXiv DOI: <https://arxiv.org/abs/1911.01254>)

Supporting information for this article is available on the WWW under <https://doi.org/10.1002/cphc.202000845>

© 2021 The Authors. ChemPhysChem published by Wiley-VCH GmbH.
This is an open access article under the terms of the Creative Commons Attribution Non-Commercial License, which permits use, distribution and reproduction in any medium, provided the original work is properly cited and is not used for commercial purposes.

1. Introduction

Water splitting has gained increased scientific interest in the past years as a sustainable source of carbon-free fuels, which could become a future alternative to the existing fossil-based sources.^[1] In particular, solar light-induced catalytic splitting of water into hydrogen and oxygen is a very promising approach to generate hydrogen as a solar fuel, which undergoes combustion without producing undesired CO_2 .^[2] Applying catalysts allows to overcome the relatively high thermodynamical barriers associated with the chemical reaction steps leading to the evolution of oxygen and hydrogen.^[3] In particular, homogeneous catalysis is rapidly emerging in this field, and various protocols for the generation of oxygen^[4] and hydrogen^[5] from water have been published. A key challenge in this area is the design of more efficient photosensitizers (PS) that absorb well visible light leading to charge-separated and long-lived electronically excited states.^[6] The latter are typically associated with strong reductive and oxidative power and have to provide negative and positive charge with sufficient driving force for enabling water reduction (hydrogen generation) and oxidation (oxygen generation), respectively. Metalorganic complexes represent a very promising class of PSs since many of them feature rather long living metal-to-ligand charge transfer triplet ($^3\text{MLCT}$) states and, therefore, are currently subject of intense research activities. While at the beginning ruthenium complexes were mostly applied, meanwhile, amongst others, iridium (Ir), copper, and iron complexes are broadly investigated. Iridium complexes such as the heteroleptic complex $[\text{Ir}^{\text{III}}(\text{ppy})_2(\text{bpy})]^+$ (where ppy = 2-phenylpyridine and bpy = 2,2'-bipyridine), turned out to be promising candidates for PSs in water splitting.^[7,8] Gärtner et al. reported that this Ir-based PS (IrPS) results, in combination with iron carbonyl complexes as

catalysts, in efficient homogenous systems for photocatalytic hydrogen generation.^[9] Under optimized conditions exceptionally high internal quantum yields exceeding 40% were achieved.^[10,11] The work on copper, iron, and other non-precious metals is driven by the goal to replace the rare noble metals by more abundant and less expensive elements. In the case of iron PSs the research is still focused on the design of complexes with suitable long-lived MLCT states.^[12–14] Promising results in photocatalytic water reduction were already reported for homogeneous photocatalytic systems based on Cu(I) PS complexes as well as on zinc porphyrins.^[15–17] However, all systems are still far from being applied in the real world due to their insufficient performance. Detailed mechanistic studies applying operando methods and stationary as well as time-resolved spectroscopy are performed in order to understand the individual reaction steps, the microscopic mechanisms, and performance limiting factors and to provide in this way guidelines for a better system design.^[18–20] Systems based on IrPSs are particularly well suited for such investigations since they show high yields and several spectroscopic experiments provide already a solid data base for the interpretation of results obtained by more sophisticated approaches.^[11,21–23]

Along this line we present the application of a suite of complementary time-resolved (TR) hard X-ray spectroscopies with picosecond (ps) temporal resolution, in combination with ab initio electronic structure calculations to study a fully functional photocatalytic system for solar hydrogen generation (Figure 1). It includes triethylamine (TEA) acting as a sacrificial reductant (SR) that quenches the photoexcited $[\text{Ir}^{\text{III}}(\text{ppy})_2(\text{bpy})](\text{PF}_6)$ and a $\text{Fe}_3(\text{CO})_{12}$ complex as the water reduction catalyst. Our study aims to complete the current picture^[22,24] of the influence of geometric and/or electronic structures of long-lived (>100 ps) charge-separated excited states on the system's performance. This includes the efficiency of light-harvesting, subsequent reductive quenching of the IrPS by the SR molecules, and the intermolecular electron transfer to the water reduction catalyst (WRC). A deeper understanding of the structure-function relationship is critical for the develop-

ment and optimization of PS complexes for efficient hydrogen production in molecular photocatalysis.

The function of this system and its constituents has been described previously in Refs. [21,24–26], cf. Figure 1. It involves a four-step process, in which the Ir-based PS absorbs a photon and is excited to an electronically excited state PS^* (step I), which can be subsequently reduced by an electron transfer from a TEA molecule yielding PS^- (step II). The next step involves another electron transfer to the WRC (step III), which then reduces a proton of a nearby H_3O^+ molecule to hydrogen (step IV). The photocatalytic reaction steps reported here are initiated by excitation in the intense metal-to-ligand charge transfer (MLCT) bands in the near UV range around 350 nm. The complete UV-Vis absorption spectrum of the IrPS complex is shown in Figure S1 of the Electronic Supplementary Information (ESI).

The photophysical and -chemical processes in IrPS, which take place upon the excitation into the singlet MLCT band at 355 nm are summarized in Figure 2. The photoexcitation of the molecule occurs within the Franck-Condon regime from the singlet ground state S_0 to a singlet MLCT state labeled S_m . The lowest excited bright state corresponds to a $\pi d_{x^2-y^2} \rightarrow \pi^*(\text{ppy})$ electronic transition.^[27,28] Excitation is followed by an ultrafast relaxation via internal conversion (IC) and intersystem crossing (ISC) into the lowest triplet MLCT state of $\pi d_{x^2-y^2} \rightarrow \pi^*(\text{bpy})$ character labeled T_1 . Recently, ISC rates for similar Ir(III)-complexes were measured using femtosecond optical transient absorption spectroscopy^[29] and TR photoluminescence measurements.^[29,30] It was found that the ISC and relaxation into T_1 state occurs within 70–100 fs. This triplet state has a long lifetime, which can be chemically tuned from some hundreds of nanoseconds to several microseconds.^[9] Once in the long-lived T_1 state, the IrPS can be reduced to a doublet D_0 state by the SR and the excess electron residing on the $\pi^*(\text{bpy})$ orbital^[28] can be transferred from the PS^- complex to the WRC, as shown in step III in Figure 1. As a competing mechanism to the reduction, a radiative or non-radiative deactivation of the T_1 back into the ground state can occur. The photoluminescence lifetimes of the T_1 state in tetrahydrofuran (THF) solution both with and without

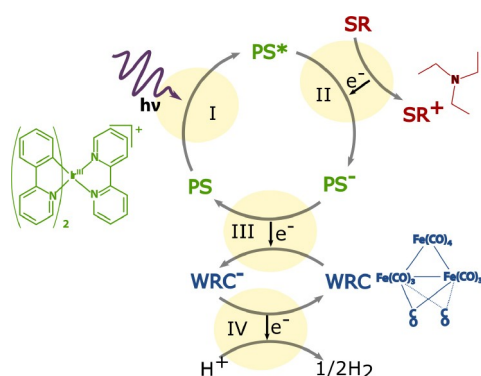


Figure 1. Reaction cycle of a photocatalytic system consisting of a homogeneous solution of a sacrificial reductant (SR), a photosensitizer (PS) and a water reduction catalyst (WRC) for solar hydrogen generation [21, 25, 9, 22, 24]. The system discussed here consists of the PS $[\text{Ir}^{\text{III}}(\text{ppy})_2(\text{bpy})]^+$, triethylamine (TEA) as the SR and $\text{Fe}_3(\text{CO})_{12}$ as the WRC.

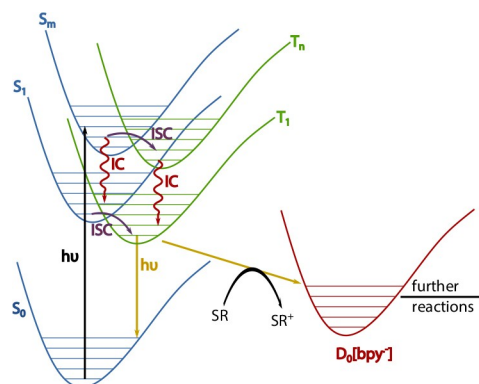


Figure 2. Potential energy surface scheme of the relevant potentials as well as the photophysical and -chemical reactions of $[\text{Ir}(\text{ppy})_2(\text{bpy})]^+$, adapted from Ref. [24]. In the present study we focus on the dynamics of the reactive T_1 state and in particular the electron transfers involving the IrPS.

the SR (present as a co-solvent in a THF/TEA mixture with a 5/1 volume ratio) were measured to be 13 ns and 370 ns, respectively.^[22]

A complete study of the underlying photoinduced dynamics and more importantly the mechanistic aspects governing these processes at the PS and the WRC sites is often severely hindered when using only optical methods, since they are not sensitive to the oxidation state of the central metal ion and the molecular geometric structure. On the contrary, employing ultrafast X-ray spectroscopies allows accessing in an element-specific manner the active sites, i.e. the different metal ions, and to capture the transient electronic and geometric structure changes occurring during the photocatalytic function of the system.

The present study is motivated by early pump-probe X-ray absorption spectroscopy (XAS) studies, in which the oxidation states^[31,32] and local geometric structures^[31–33] of liquid-phase molecular systems have been investigated. Later, TR XAS has been used to investigate the triplet excited state of the Ir model system Ir(ppy)₃^[34] and the combination with DFT allowed the study of this excited state of a pure solvated Ir photosensitizer.^[35] Picosecond- and femtosecond-resolved X-ray studies of a bimetallic donor-acceptor Ru–Co complex (a prototypical photocatalytic system) have shown how ultrashort hard X-ray spectroscopies can be efficiently used to follow both the intra- and intermolecular charge transfer processes at the optically silent sites of photocatalysts.^[36,37] In a similar study, pump-probe XAS, paired with all-optical experiments, was used to investigate intramolecular electron transfer processes in a whole family of homo- and heterodinuclear Cu(I)/Ru(II) complexes.^[38] The applicability of high-energy resolution fluorescence detection (HERFD)^[39] XAS as well as X-ray Emission Spectroscopy (XES) to answer questions in catalysis has been further demonstrated using Fe complexes.^[40] In very recent experiments, the structural and electronic configurations of a Co^[41] and Ni^[42] proton reduction catalyst were characterized.

By a similar approach we investigate here the primary electron transfer step that is experienced by the IrPS [Ir^{III}(ppy)₂(bpy)]⁺ in the above introduced photocatalytic system after optical excitation. The goal is to characterize the electronic configuration of the IrPS prior and after the electron transfer event and to identify the involved orbitals in order to obtain a validated microscopic picture of this crucial step.

Experimental Measurements

Time-resolved spectra of the X-ray absorption near edge structure (XANES) of [Ir(ppy)₂(bpy)]⁺ were collected at the 7ID–D beamline of the Advanced Photon Source (APS) both in total fluorescence yield (TFY) as well as in the HERFD mode. More details concerning the experimental setup and the pump-probe techniques available at this beamline can be found in Refs [33,43,44]. Here we will only briefly summarize the experimental conditions present during the pump-probe measurements, which allowed us to record high quality X-ray absorption and X-ray emission spectra of both the ground and excited states of the IrPS complex. The APS in 24 bunch mode delivered an average X-ray flux of 4×10^{11} photons/s at the Ir L₃-edge (11.2 keV) in pulses with a repetition rate of 6.5 MHz. The X-

ray probe pulses were monochromatized to $\Delta E/E = 5 \times 10^{-5}$ and focused to a spot of $4 \times 5 \mu\text{m}^2$ on the sample consisting of the sample solution in a 100 μm thick free flowing liquid jet. The optical pump laser repetition rate was set to 931 kHz, i.e. the 7th sub-harmonic of the X-rays. The inter-pulse spacing of 1.07 μs allows for a full ground state recovery between consecutive laser pulses. The laser wavelength was frequency tripled to 355 nm and laser pulses with 142 nJ energy were used to excite the sample. The laser focus was set to $13 \times 21 \mu\text{m}^2$, thus slightly larger than the X-ray spot size, leading to a laser peak intensity of 6.6 GW/cm². TFY XAS were measured using a scintillation detector. Simultaneously HERFD XAS were acquired to obtain XAS with sub core-hole lifetime limited energy resolution, which in simplified words works as follows: X-ray absorption spectra measured in total fluorescence yield are broadened by a total Lorentzian lifetime broadening $\Gamma = \Gamma_L + \Gamma_M$, where Γ_L and Γ_M are the lifetime widths of the intermediate and final states, in our case with an L-shell and M-shell core-hole, respectively. The intermediate state lifetime broadening Γ_L can be partially eliminated by using a detection method with a resolution better than Γ_L .^[39] The HERFD XAS were measured with a Johann^[45] spectrometer employing a Ge(800) analyzer crystal to selectively detect photons at the L α_1 peak energy of 9175 eV. Three different sample solutions were measured: i) 15 mM of pure IrPS in CH₃CN, ii) 15 mM of IrPS in a 1:4 mixture of TEA and CH₃CN and iii) 12.5 mM IrPS and 9 mM Fe₃(CO)₁₂ in a 1:5 mixture of TEA and CH₃CN. Here, CH₃CN is chosen as solvent since it is, in contrast to the THF used in the optimized catalytic system, not considered a possible carcinogen. It was previously shown that the photocatalytic system works also with CH₃CN as solvent, however, with lower yields.^[10] The high IrPS concentration is necessary due to the thin sample thickness.

Ultrafast optical absorption studies as well as time-resolved luminescence measurements were already performed on IrPS dissolved in acetonitrile.^[23] They showed that also in this Ir complex the MLCT state is populated within the first 100 fs and the lifetime of its luminescence amounts to 60 ns. Since these experiments were carried out with air-saturated samples it was advantageous for a comparison on common ground to use also in the present experiments air-saturated solutions.

Theoretical Calculations

X-ray spectra originating from the ground singlet S_0 and first excited triplet T_1 electronic states were calculated in the dipole approximation at the first principles restricted active space self-consistent field (RASSCF) level and perturbative LS-coupling scheme for the spin-orbit coupling.^[46,47] This method, due to its correlated nature, is a prerequisite to describe X-ray absorption resulting from excited states (here T_1). A relativistic ANO-RCC basis set^[48,49] of triple-zeta quality for iridium and its first coordination shell and of double-zeta quality for other atoms was employed. For the detailed description of the protocol, see e.g. Ref. [50]. The complex has a low C_2 point group symmetry. Thus, we prefer not to use octahedral symmetry labels. The active space comprised three Ir 2p, two pairs of highly correlated bonding σ d and antibonding σ^*d orbitals, the $\pi d_{x^2-y^2}$ orbital, two mainly non-bonding d_{xz} and d_{yz} orbitals, and one $\pi^*(bpy)$ orbital (see Figure 5b)). This allows for the description of the S_0 and T_1 states (originating from $\pi d_{x^2-y^2} \rightarrow \pi^*(bpy)$ excitation) as well as of the Ir L-edge core excited states. The influence of solvent was not taken into account. This setup should provide reliable results for transition metal compounds, where static electron correlation could play an important role.^[27] Spectra were calculated at the equilibrium geometries of the S_0 and T_1 states taken from Ref. [27]. Molecular orbital energies were obtained using long-range corrected density

functional theory (LC-BLYP with a LANL2DZ/6-31G(d) basis set)^[51] since RASSCF does not provide energies of canonical orbitals.

2. Results and Discussion

Figure 3 shows the TFY and HERFD XANES spectra of bare IrPS in CH₃CN (i.e. in absence of TEA and WRC) with and without laser excitation, as well as the transient difference between laser excited and GS and the reconstructed excited state spectrum. The spectrum of the laser excited sample (Laser ON) was determined to contain an excited state fraction of 12%. This is used to reconstruct the excited state (ES) spectrum by removing the remaining (dominant) contribution of the ground state (GS) from the laser excited spectrum. See ESI for details on the determination of the excited state fraction and the reconstruction of the excited state spectrum.

The features of the TFY spectra are extremely broad due to the 5.25 eV L₃-edge core-hole lifetime broadening.^[52] The HERFD spectra show the same features as the TFY spectra, however, with a by about 2 eV improved resolution of 3.0–3.5 eV. Thus

for the further analysis we focus on the HERFD spectra in Figure 3b). The prominent features of the spectra are labeled A, B and C, cf. Table 1. In the GS spectrum a very intense white line feature B around 11.219 keV and a second transition C at higher energy of about 11.229 keV are visible. The ES spectrum contains an additional peak A at a lower energy of about 11.215 keV, which is not visible in the GS spectra. Furthermore, B and C shift about 1 eV – 2 eV to higher energies in the ES compared to the GS, thus evidencing the oxidation of the Ir center from Ir^{III} to Ir^{IV}.

The L₂-edge measured in TFY is presented in Figure 4a) and exhibits the same features in the GS as the L₃-edge. However, in the ES the feature A is not clearly visible, only an extremely weak shoulder could potentially be observed here. Even when comparing the transient differences of the GS and the ES (see Figure 4b), in the L₂-edge the first positive peak, which is very pronounced in the L₃-edge, is not present.

The assignment of the L₃-edge features is made on the basis of RASSCF calculations. The comparison of the experimental and theoretical spectra for both ground and excited states can be found in Figure 5a). The spectrum consists of several tens of transitions with non-zero intensity. Some of them have minute contributions but sum up to a notable feature due to their number. The assignment of multi-reference many-body RASSCF

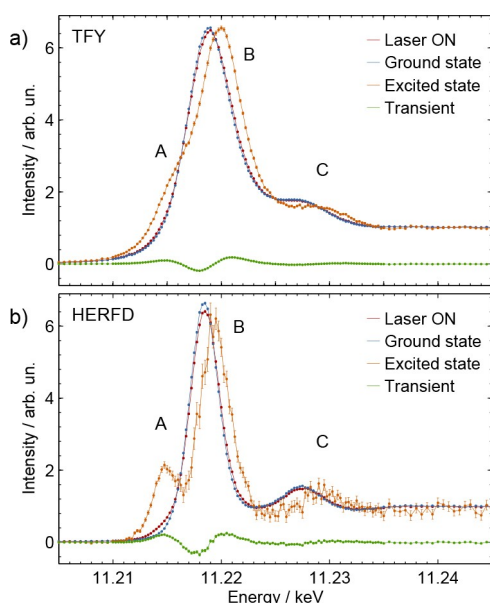


Figure 3. L₃-edge XANES spectra measured in a) TFY and b) HERFD of the laser excited ensemble (red), the ground state (blue), the reconstructed excited state (orange) and the transient difference between laser excited and GS (green) of Ir[(ppy)₂(bpy)]⁺ in CH₃CN.

Table 1. Upper panel: Energies of L₃-edge XANES features, all energies are given in eV relative to the 2p_{3/2} ionization energy of 11215 eV. Lower panel: Energies of L₂-edge XANES features, all energies are given in eV relative to the 2p_{1/2} ionization energy of 12824 eV.

	A	B	C	edge
Ground state (L ₃)		3.8 ± 0.1	12.8 ± 0.3	5.4 ± 1.6
Excited state (L ₃)	0.2 ± 0.2	4.8 ± 0.3	14.7 ± 0.4	6.4 ± 8.8
Shift GS-ES (L ₃)		+1.0 ± 0.4	+1.9 ± 0.5	+1.0 ± 9.0
Ground state (L ₂)		2.7 ± 0.1	11.7 ± 0.1	4.5 ± 1.1
Excited state (L ₂)	−0.8 ± 0.4	3.7 ± 0.2	13.4 ± 0.3	5.7 ± 3.3
Shift GS-ES (L ₂)		+1.0 ± 0.3	+1.7 ± 0.4	+1.2 ± 3.5

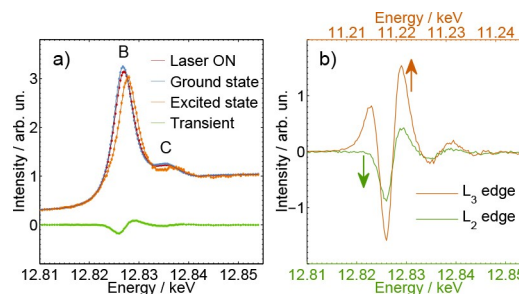


Figure 4. a) TFY L₂-edge XANES of the laser excited ensemble (red), the reconstructed excited state (orange), the ground state (blue) and the transient difference between laser excited and GS (green) of Ir[(ppy)₂(bpy)]⁺ in CH₃CN. In b), a comparison between this L₂-edge transient (green) to the L₃-edge transient (orange) is shown, the transients are normalized to the respective edge jump and scaled to 100% excited state fraction.

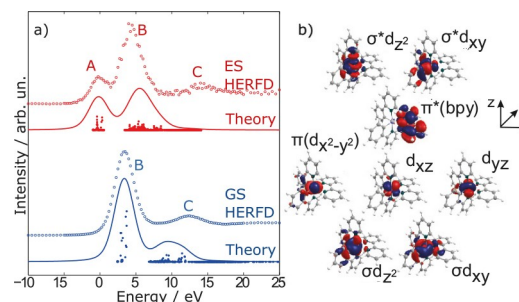


Figure 5. a) Simulated (theory) and measured HERFD L₃-edge XANES of the S₀ GS (blue, bottom) and the T₁ MLCT ES (red, top). The x-axis is given relative to the 2p_{3/2} ionization energy of 11215 eV, features A, B and C are labeled as in Figure 3. b) Orbital active space (apart from 2p orbitals) used for the RASSCF calculations.

wave functions is quite involved due to their multiconfigurational character, which is additionally complicated by spin-orbit coupling. Here, for simplicity, the information is reduced to transitions between single orbitals (Figure 5b)), having however non-integer occupations. An orbital energy scheme for the relevant transitions discussed in the following is given in Figure 6).

The GS spectrum contains two features denoted as B and C in Figure 5a) (blue line). Peak B mainly consists of $2p \rightarrow \sigma^*d_{z^2}$ and $2p \rightarrow \sigma^*d_{xy}$ transitions. Remarkably, some of the transitions having non-vanishing intensity are of $2p \rightarrow \pi^*(bpy)$ nature and can be considered as charge-transfer excitations. Peak C in turn is due to two-electron shake up transitions, where in the region of 7–10 eV $2p \rightarrow \sigma^*d_{z^2}$ transitions are occurring simultaneously with excitations from $\pi d_{x^2-y^2}$ and d_{xz} orbitals to $\pi^*(bpy)$ ones. Transitions in the 10–13 eV range are very similar but in this case σ^*d_{xy} is accepting the electron instead of $\sigma^*d_{z^2}$.

Features in the T_1 spectrum have similar nature as those of the ground state spectrum with the only difference that the triplet configuration has a hole in the $\pi d_{x^2-y^2}$ orbital and an additional electron in the $\pi^*(bpy)$ orbital. This fact gives rise to an additional feature A in the excited state spectrum where transitions correspond mainly to $2p \rightarrow \pi d_{x^2-y^2}$ excitation. This

assignment is in agreement with that reported for the higher symmetric homoleptic $[Ru(bpy)_3]^{2+}$ complex.^[31] The main type of transitions contributing to feature B is of $2p \rightarrow \sigma^*d_{z^2}$ and $2p \rightarrow \sigma^*d_{xy}$ nature. In addition to shake ups mentioned above, one sees also contributions from $d_{xz,yz} \rightarrow \pi d_{x^2-y^2}$ and $\pi^*(bpy) \rightarrow \sigma^*d_{xy}$ transitions because of the additional hole/electron present in the T_1 state. Interestingly, the low-energy flanks of the bands A and B in the T_1 spectrum have mainly spin-forbidden character gaining intensity due to spin-orbit coupling. This means that the initial state is mostly triplet, while the final ones are predominantly singlet. According to the calculations, the $2p_{1/2} \rightarrow \pi d_{x^2-y^2}$ transitions corresponding to the A feature in the L_2 band are not energetically separated from the transitions constituting the B band. Moreover, they have a significantly lower intensity than for the L_3 -edge. Both energetic blue shift and low intensity are due to the notable two-electron excitation character of the respective states, making them a mixture of the main and shake-up transitions.

To further quantify the exact energy positions of the XAS features, the HERFD XANES spectra have been fitted using a superposition of an arctan-broadened absorption edge and Voigt profiles for the discrete transitions. The corresponding bands of the fit are shown in Figure 6a) and b) and the peak and edge position obtained from this fit can be found in Table 1. The same fitting procedure was also applied to the L_2 -edge TFY XAS (see ESI). Here, although not clearly visible at first sight, also a transition A had to be included. The obtained energies of the respective features are added to the table. The energy shift between the A and B transitions reflects the energy difference between the $\pi d_{x^2-y^2}$ and the two σ^* orbitals of (4.6 ± 0.4) eV which is within the error bars also confirmed by the respective features of the L_2 -edge. The splitting is in good accord with the theoretical value reported in Figures 5a and 6c. Most importantly for the application of the time-resolved XAS measurements to the catalytic hydrogen production process, we are able to determine the occupation of the 5d-orbital and to monitor the optically induced charge separation with concomitant creation of a vacancy in the 5d-shell. This should in the next step allow for monitoring the arrival of an additional charge from the SR to the PS^* .

The static TFY XANES spectra of the IrPS in CH_3CN , of the IrPS in the TEA/ CH_3CN mixture and of the IrPS in the mixture together with the WRC $Fe_3(CO)_{12}$ are indistinguishable within our experimental accuracy, see Figure 7. This allows us to conclude that the addition of the SR as well as of the WRC does not severely affect the geometric or electronic structure of the IrPS in the GS. The transient TFY XANES of all three samples after optical excitation are qualitatively similar as well, thus 100 ps after photoexcitation the IrPS is presumably in the same electronic state independent of the addition of the SR and the WRC.

Time delay scans of the excited state of these three samples have been taken at the energy of maximum transient intensity, i.e. at 11221.5 eV (see Figure 8). A fit of a convolution of a Gaussian broadened step function with an exponential decay delivered MLCT excited state lifetimes of (39.6 ± 2.8) ns, (5.0 ± 0.6) ns and (6.7 ± 0.7) ns for the IrPS in CH_3CN , the IrPS in the

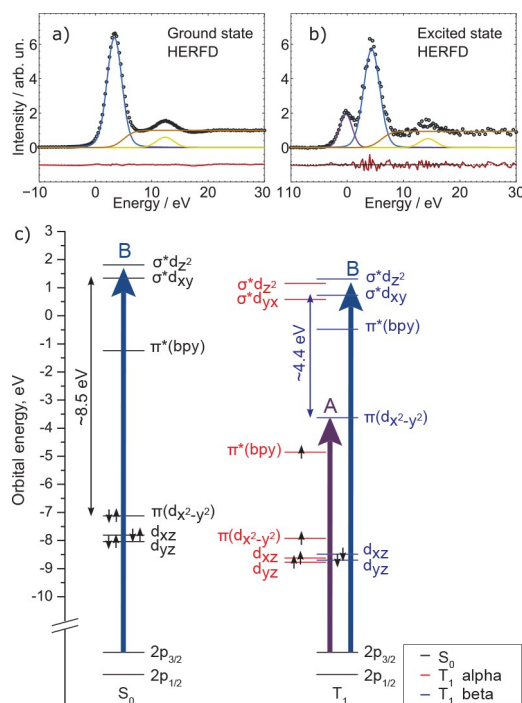


Figure 6. Reconstructed HERFD XANES spectra together with measured data of $[Ir(ppy)_2(bpy)]^+$ in CH_3CN in its GS a) and ES b). The x-axis is given relative to the $2p_{3/2}$ ionization energy of 11215 eV. c) Diagram showing the relevant orbitals as computed with restricted (S_0) and unrestricted (T_1) density functional theory. The orbital manifold of the T_1 state contains two subsets: α orbitals occupied by spin-up electrons (red) and β ones with spin-down electrons (blue) which have different energies. The transitions of the L_3 -edge for the GS involve the orbitals $2p_{3/2}$, $\sigma^*d_{z^2}$, and σ^*d_{xy} (blue arrow band B) and for the ES additionally transition to spin-down $\pi d_{x^2-y^2}$ (purple arrow, band A). The L_2 -edge XANES contains the corresponding transitions starting from the $2p_{1/2}$ sub-shell (not shown with arrows).

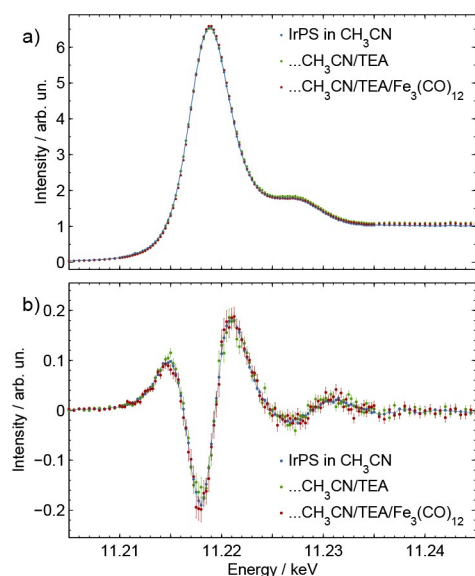


Figure 7. Comparison of the TFY yield L₃-edge XANES of [Ir(ppy)₂(bpy)]⁺ in CH₃CN (blue), as well as in CH₃CN/TEA (green) and in CH₃CN/TEA/Fe₃(CO)₁₂ (red) mixtures, respectively. In a) the ground state spectra and in b) the transient differences 100 ps after excitation are shown. The static spectra and the transient differences are arbitrarily scaled in intensity to simplify comparison.

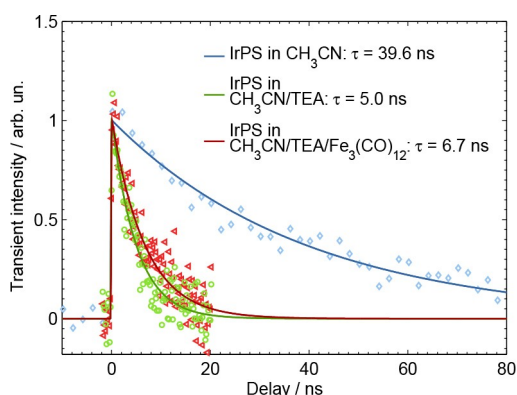


Figure 8. Time delay scan of the transient difference XANES intensity at 11221.5 eV of [Ir(ppy)₂(bpy)]⁺ in CH₃CN (blue), as well as in CH₃CN/TEA (green) and CH₃CN/TEA/Fe₃(CO)₁₂ (red) mixtures. A fit of an exponential decay represents the excited state lifetimes of (39.6 ± 2.8) ns, (5.0 ± 0.6) ns and (6.7 ± 0.7) ns for the three samples, respectively.

TEA/CH₃CN mixture and the IrPS together with the Fe₃(CO)₁₂ in the TEA/CH₃CN mixture, respectively. The ground state recovery time of (39.6 ± 2.8) ns is similar, but slightly shorter than the previously reported luminescence decay time of 60 ns, which is supposed to reflect the depopulation of the MLCT state into the ground state.^[23] The shorter ground state recovery could be due to the relatively high concentration of IrPS leading to self-quenching. The lifetime shortening associated with the addition of TEA by a factor of 8 is due to the electron transfer (ET) from TEA to the IrPS, see step II in Fig. 1. The MLCT state is clearly observed via the appearance of the A feature and the shift of the strong B transition upon optical excitation and the

associated depopulation of the $\pi d_{x^2-y^2}$ -orbital. The lifetime of this transiently formed Ir^{IV} center of the MLCT state is probed representatively at the B-feature, although a more intuitive probe for future experiments could be to directly monitor the $\pi d_{x^2-y^2}$ -orbital filling via the A feature. Furthermore, the observed changes in the spectral features can be mainly attributed to the change in the oxidation state of Ir, and are not sensitive to the additional electron residing on the bpy ligand after the ET from TEA. This is supported by theory as $\pi^*(bpy) \rightarrow \sigma^* d_{x^2-y^2}$ and $\sigma^* d_{xy}$ transitions as a rule have negligible intensity. The slightly longer excited state lifetime of 7 ns in the fully functionally photocatalytic system can be attributed to the lower TEA concentration. Also in the presence of the WRC, the electron transfer from TEA is responsible for filling the hole at the Ir atom and oxidative quenching plays no role. Using the ES lifetime τ_0 without and τ with the TEA present we can estimate the TEA concentration c_{TEA} dependent quenching rate constant k_q of the ES via ET using the Stern-Volmer equation^[53]

$$k_q(c_{TEA}) = \frac{1}{\tau} - \frac{1}{\tau_0} \approx 1.76 \times 10^8 \text{ s}^{-1}. \quad (1)$$

With the TEA concentration $c_{TEA} = 1.44 \text{ M}$ this results in a bimolecular quenching ET rate of $k_{ET} = 1.22 \times 10^8 \text{ M}^{-1} \text{ s}^{-1}$. The ET rate for a diffusion limited reaction is estimated to $2.06 \times 10^{10} \text{ M}^{-1} \text{ s}^{-1}$ (see ESI for details). The estimate of both the quenching rate constant and the diffusion limited ET rate rely on the prior knowledge that the reaction is of first order,^[22] for a more rigorous analysis, multiple data points at distinct TEA concentrations should be taken. According to the findings, only about every 170th encounter of a TEA molecule with an excited IrPS leads to an electron transfer process.

The results are well in line with previous findings obtained by time-resolved photoluminescence measurements on the IrPS. In that case quenching of the sensitizer phosphorescence by TEA was studied in tetrahydrofuran solutions.^[22] A bimolecular quenching rate of $5.9 \times 10^7 \text{ M}^{-1} \text{ s}^{-1}$ was observed while the diffusion controlled collision rate was estimated to $1.4 \times 10^{10} \text{ M}^{-1} \text{ s}^{-1}$ indicating that only one out of 200 collisions results in a quenching event. This is in good agreement with the ET efficiency found in the present experiments. In the previous study also ab initio calculations on the collision complex were performed.^[22] They indicate that only at specific collision geometries an ET is possible and only a small fraction of the collisions occurs with such a geometry. This can explain the small number of encounters resulting in ET. The advantage of the present measurements is that not only depopulation of a luminescent state is observed but rather a transiently generated Ir^{IV} center, as part of the MLCT excited state, and the subsequent electron transfer from TEA to the 5d-orbital of Ir, changing its oxidation state back to +3, thus proving the proposed ET pathway.

3. Conclusions

We have applied picosecond-resolved X-ray spectroscopies to investigate an Ir-based PS for photocatalytic hydrogen generation. We were able to quantify the electronic structural changes of the PS as they take place during the photocatalytic cycle by mapping the (metal centered) unoccupied orbitals of the IrPS in ground and excited states using mainly L_3 -edge XANES. The features in the TFY spectra are extremely broadened due to the >5 eV core-hole lifetime and applying HERFD XANES enabled an improvement in resolution of about 2 eV down to 3.0 eV–3.5 eV. This allowed for an accurate analysis of the XANES features and decomposing the edge into its main transitions, i.e. to accurately determine their energy positions and relative intensities. The detailed analysis was guided by high-level *ab initio* calculations of ground and excited state spectra. Equipped with this knowledge about relevant X-ray fingerprints, the IrPS in the fully functioning photocatalytic system was investigated. Here, we were able to directly observe the bimolecular electron transfer process from TEA to the IrPS via a reduction of the MLCT excited state lifetime of the IrPS by a factor of about 8. More specifically, we can monitor the oxidation state of the Ir atom. After optical excitation and trapping in the MLCT state, the Ir^{III} ion is oxidized to Ir^{IV} leading to the appearance of a new band in the X-ray absorption spectrum. Upon bimolecular electron transfer from the sacrificial reductant the hole on the Ir 5d shell is refilled, yielding back Ir^{III} and its characteristic spectrum. Due to the element specificity the extra electron on the bpy ligand does not yield noticeable changes in the Ir L-edge spectrum. Hence, the present setup is not sensitive to the electron relay from the IrPS to the WRC. Therefore, in future studies it would be desirable to also apply time-resolved X-ray absorption and emission at the Fe-edges of the WRC ($\text{Fe}_3(\text{CO})_{12}$) to monitor also the last steps (III and IV) of the reaction cycle.

To summarize, the present proof-of-principle study has enhanced our understanding of functionally relevant bimolecular electron transfer reactions and thus will pave the road to rational optimization of the performance of homogeneous photocatalytic systems.

Author Contributions

WG, CB, OK, SL and AB designed the research; NR and HJ synthesized the sample; NR, HJ and MB contributed to the conception; GD, AMM and SHS built the high-repetition rate pump-probe X-ray spectroscopy setup; AB, TA, EGB, ZN, GV, GD, AMM and SHS performed the X-ray experiments; SIB performed the simulations; AB analyzed the experimental data; AB, SIB and WG wrote the manuscript with contributions from all co-authors.

Acknowledgements

We thank Chris Milne and Jakub Szlachetko for their help with setting up the HERFD XAS measurements and for the loan of analyzer crystals, Frank de Groot and Pieter Glatzel for discussions regarding the interpretation of the HERFD XAS measurements as

well as Daniel Haskel for the loan of the Ir(IV) reference. This work is financed by the European XFEL, by the Deutsche Forschungsgemeinschaft (DFG, German Research Foundation) via SFB925 – project 170620586 (Teilprojekt A4), and by the Clusters of Excellence “Center for Ultrafast Imaging” (CUI, EXC 1074, ID 194651731) and “Advanced Imaging of Matter” (AIM, EXC 2056, ID 390715994) of the Deutsche Forschungsgemeinschaft (DFG). AB acknowledges support from the International Max Planck Research School for Ultrafast Imaging and Structural Dynamics (IMPRS-UFAST). ZN, ÉGB and GV from the Wigner-Lendület’ (Momentum) Femtosecond Spectroscopy Research Group were supported by the ELKH under contract LP2013-2/2020 Program of the Hungarian Academy of Sciences (LP2013-59), the Government of Hungary and the European Regional Development Fund under grant VEKOP-2.3.2-16-2017-00015, and the National Research, Development and Innovation Fund (NKFIH) under contract FK124460. SIB and OK acknowledge financial support from DFG (grants BO 4915/1-1 and KU 952/10-1). GD, AMM and SHS were supported by the US Department of Energy, Office of Science, Office of Basic Energy Sciences, Chemical Sciences, Geosciences and Biosciences Division under award number DE-AC02-06CH11357. W.G. acknowledges partial funding from Narodowe Centrum Nauki through SONATA BIS 6 grant (2016/22/E/ST4/00543). W.G. further acknowledges funding from Spanish MIU through “Ayudas Beatriz Galindo” (BEAGAL18/00092), Comunidad de Madrid and Universidad Autónoma de Madrid through “Proyecto de I+D para Investigadores del Programa Beatriz Galindo” (SI2/PBG/2020-00003), Spanish MICIU through “Proyecto de I+D+i 2019” (PID2019-108678GB-I00) and IMDEA-Nanociencia through Severo Ochoa Programme in R&D (SEV-2016-0686). This research used resources of the Advanced Photon Source, a U.S. Department of Energy (DOE) Office of Science User Facility operated for the DOE Office of Science by Argonne National Laboratory under Contract No. DE-AC02-06CH11357. Open access funding enabled and organized by Projekt DEAL.

Conflict of Interest

The authors declare no conflict of interest.

Keywords: homogeneous catalysis • photocatalytic water splitting • electron transfer • x-ray absorption spectroscopy • high energy-resolution • fluorescence detection XAS • ultrafast XAS • restricted active space self-consistent field calculations

- [1] N. Armaroli, V. Balzani, *Angew. Chem. Int. Ed.* **2007**, 46, 52–66; *Angew. Chem.* **2007**, 119, 52–67.
- [2] N. S. Lewis, D. G. Nocera, *Proc. Natl. Acad. Sci. USA* **2006**, 103, 15729–15735.
- [3] K. Sanderson, *Nature* **2008**, 452, 400–402.
- [4] X. Sala, I. Romero, M. Rodríguez, L. Eiche, A. Llobet, *Angew. Chem. Int. Ed.* **2009**, 48, 2842–2852; *Angew. Chem.* **2009**, 121, 2882–2893.
- [5] M. Wang, Y. Na, M. Gorlov, L. Sun, *Dalton Trans.* **2009**, 6458–6467.
- [6] O. Bokareva, T. A. Neubauer, S. Bokarev, S. Lochbrunner, O. Kühn, *Inorganics* **2017**, 5, 23.
- [7] J. I. Goldsmith, W. R. Hudson, M. S. Lowry, T. H. Anderson, S. Bernhard, *J. Am. Chem. Soc.* **2005**, 127, 7502–7510.

- [8] L. L. Tinker, N. D. McDaniel, P. N. Curtin, C. K. Smith, M. J. Ireland, S. Bernhard, *Chem. Eur. J.* **2007**, *13*, 8726–8732.
- [9] F. Gärtner, S. Denurra, S. Losse, A. Neubauer, A. Boddien, A. Gopinathan, A. Spannenberg, H. Junge, S. Lochbrunner, M. Blug, S. Hoch, J. Busse, S. Gladiali, M. Beller, *Chem. Eur. J.* **2012**, *18*, 3220–3225.
- [10] F. Gärtner, D. Cozzula, S. Losse, A. Boddien, G. Anilkumar, H. Junge, T. Schulz, N. Marquet, A. Spannenberg, S. Gladiali, M. Beller, *Chem. Eur. J.* **2011**, *17*, 6998–7006.
- [11] H. Junge, N. Rockstroh, S. Fischer, A. Brückner, R. Ludwig, S. Lochbrunner, O. Kühn, M. Beller, *Inorganics* **2017**, *5*, 14.
- [12] O. S. Wenger, *Chem. Eur. J.* **2019**, *25*, 6043–6052.
- [13] P. Zimmer, L. Burkhardt, A. Friedrich, J. Steube, A. Neuba, R. Schepper, P. Müller, U. Flörke, M. Huber, S. Lochbrunner, M. Bauer, *Inorg. Chem.* **2018**, *57*, 360–373.
- [14] T. C. B. Harlang, Y. Liu, O. Gordivska, L. A. Fredin, C. S. Ponseca, P. Huang, P. Chábera, K. S. Kjaer, H. Mateos, J. Uhlig, R. Lomoth, R. Wallenberg, S. Styring, P. Persson, V. Sundström, K. Wärnmark, *Nat. Chem.* **2015**, *7*, 883–889.
- [15] S.-M. Kuang, D. G. Cuttall, D. R. McMillin, P. E. Fanwick, R. A. Walton, *Inorg. Chem.* **2002**, *41*, 3313–3322.
- [16] T. Lazarides, M. Delor, I. V. Sazanovich, T. M. McCormick, I. Georgakaki, G. Charalambidis, J. A. Weinstein, A. G. Coutsolelos, *Chem. Commun.* **2014**, *50*, 521–523.
- [17] B. J. McCullough, B. J. Neyhouse, B. R. Schrage, D. T. Reed, A. J. Osinski, K. J. Ziegler, T. A. White, *Inorg. Chem.* **2018**, *57*, 2866–2875.
- [18] S. Fischer, D. Hollmann, S. Tschierlei, M. Karnahl, N. Rockstroh, E. Barsch, P. Schwarzbach, S.-P. Luo, H. Junge, M. Beller, S. Lochbrunner, R. Ludwig, A. Brückner, *ACS Catal.* **2014**, *4*, 1845–1849.
- [19] D. M. Arias-Rotondo, J. K. McCusker, *Chem. Soc. Rev.* **2016**, *45*, 5803–5820.
- [20] A. Pöpcke, A. Friedrich, S. Lochbrunner, *J. Phys. Condens. Matter* **2020**, *32*, 153001.
- [21] F. Gärtner, B. Sundararaju, A. E. Surkus, A. Boddien, B. Loges, H. Junge, P. H. Dixneuf, M. Beller, *Angew. Chem. Int. Ed.* **2009**, *48*, 9962–9965; *Angew. Chem.* **2009**, *121*, 10147–10150.
- [22] A. Neubauer, G. Grell, A. Friedrich, S. I. Bokarev, P. Schwarzbach, F. Gärtner, A.-E. Surkus, H. Junge, M. Beller, O. Kühn, S. Lochbrunner, *J. Phys. Chem. Lett.* **2014**, *5*, 1355–1360.
- [23] S. Tschierlei, A. Neubauer, N. Rockstroh, M. Karnahl, P. Schwarzbach, H. Junge, M. Beller, S. Lochbrunner, *Phys. Chem. Chem. Phys.* **2016**, *18*, 10682–10687.
- [24] S. I. Bokarev, O. S. Bokareva, O. Kühn, *Coord. Chem. Rev.* **2015**, *304*–*305*, 133–145.
- [25] F. Gärtner, A. Boddien, E. Barsch, K. Fumino, S. Losse, H. Junge, D. Hollmann, A. Brückner, R. Ludwig, M. Beller, *Chem. Eur. J.* **2011**, *17*, 6425–6436.
- [26] S. Fischer, O. S. Bokareva, E. Barsch, S. I. Bokarev, O. Kühn, R. Ludwig, *ChemCatChem* **2016**, *8*, 404–411.
- [27] S. I. Bokarev, O. S. Bokareva, O. Kühn, *J. Chem. Phys.* **2012**, *136*, 214305.
- [28] S. I. Bokarev, D. Hollmann, A. Pazidis, A. Neubauer, J. Radnik, O. Kühn, S. Lochbrunner, H. Junge, M. Beller, A. Brückner, *Phys. Chem. Chem. Phys.* **2014**, *16*, 4789–4796.
- [29] G. J. Hedley, A. Ruseckas, I. D. W. Samuel, *J. Phys. Chem. A* **2009**, *113*, 2–4.
- [30] E. Pomarico, M. Silatani, F. Messina, O. Braem, A. Cannizzo, E. Barranoff, J. H. Klein, C. Lambert, M. Chergui, *J. Phys. Chem. C* **2016**, *120*, 16459–16469.
- [31] W. Gawelda, M. Johnson, F. M. F. De Groot, R. Abela, C. Bressler, M. Chergui, *J. Am. Chem. Soc.* **2006**, 5001–5009.
- [32] L. X. Chen, G. B. Shaw, E. C. Wasinger, X. Zhang, K. Attenkofer, G. Jennings, *AlP Conf. Proc.* **2007**, *882*, 844–848.
- [33] G. Vankó, A. Bordage, M. Pápai, K. Haldrup, P. Glatzel, A. M. March, G. Doumy, A. Britz, A. Galler, T. A. Assefa, D. Cabaret, T. B. V. Driel, K. S. Kjaer, A. O. Dohn, K. B. Møller, H. T. Lemke, M. Rovezzi, Z. Németh, E. Rozsályi, T. Rozgonyi, J. Uhlig, V. Sundström, M. M. Nielsen, L. Young, S. H. Southworth, C. Bressler, W. Gawelda, *J. Phys. Chem. C* **2015**, *119*, 5888–5902.
- [34] D. Goeries, Ph.D. thesis, Uni Hamburg, **2014**.
- [35] G. Smolentsev, L. M. van Vliet, A. Nicolo Azzaroli, J. A. van Bokhoven, A. M. Brouwer, B. de Bruin, M. Nachtegaal, M. Tromp, *Photochem. Photobiol. Sci.* **2018**, *17*, 896–902.
- [36] S. Canton, X. Zhang, J. Zhang, T. B. van Driel, K. S. Kjaer, K. Haldrup, P. Chabera, T. Harlang, K. Suarez-Alcantara, Y. Liu, J. Pérez, A. Bordage, M. Pápai, G. Vankó, G. Jennings, C. A. Kurtz, M. Rovezzi, P. Glatzel, G. Smolentsev, J. Uhlig, A. O. Dohn, M. Christensen, A. Galler, W. Gawelda, C. Bressler, H. T. Lemke, K. B. Møller, M. M. Nielsen, R. Lomoth, K. Wärnmark, V. Sundström, *J. Phys. Chem. Lett.* **2013**, *4*, 1972–1976.
- [37] S. E. Canton, K. S. Kjaer, G. Vankó, T. B. van Driel, S.-I. Adachi, A. Bordage, C. Bressler, P. Chabera, M. Christensen, A. O. Dohn, A. Galler, W. Gawelda, D. Gosztola, K. Haldrup, T. Harlang, Y. Liu, K. B. Møller, Z. Németh, S. Nozawa, M. Papai, T. Sato, T. Sato, K. Suarez-Alcantara, T. Togashi, K. Tono, J. Uhlig, D. A. Vithanage, K. Wärnmark, M. Yabashi, J. Zhang, V. Sundström, M. M. Nielsen, *Nat. Commun.* **2015**, *6*, 359.
- [38] D. Hayes, L. Kohler, R. G. Hadt, X. Zhang, C. Liu, K. L. Mulfort, L. X. Chen, *Chem. Sci.* **2018**, *9*, 860–875.
- [39] K. Hämäläinen, D. Siddons, J. Hastings, L. Berman, *Phys. Rev. Lett.* **1991**, *67*, 2850–2853.
- [40] M. Bauer, *Phys. Chem. Chem. Phys.* **2014**, *16*, 13827–13837.
- [41] D. Moonshiram, C. Gimbert-Surinach, A. Guda, A. Picon, C. S. Lehmann, X. Zhang, G. Doumy, A. M. March, J. Benet-Buchholz, A. Soldatov, A. Llobet, S. H. Southworth, *J. Am. Chem. Soc.* **2016**, *138*, 10586–10596.
- [42] D. Moonshiram, A. Guda, L. Kohler, A. Picon, S. Guda, C. S. Lehmann, X. Zhang, S. H. Southworth, K. L. Mulfort, *J. Phys. Chem. C* **2016**, *120*, 2004920057.
- [43] A. M. March, A. Stickrath, G. Doumy, E. P. Kanter, B. Krässig, S. H. Southworth, K. Attenkofer, C. A. Kurtz, L. X. Chen, L. Young, *Rev. Sci. Instrum.* **2011**, *82*, 73110.
- [44] K. Haldrup, G. Vankó, W. Gawelda, A. Galler, G. Doumy, A. M. March, E. P. Kanter, A. Bordage, A. Dohn, T. B. van Driel, K. S. Kjaer, H. T. Lemke, S. E. Canton, J. Uhlig, V. Sundström, L. Young, S. H. Southworth, M. M. Nielsen, C. Bressler, *J. Phys. Chem. A* **2012**, *116*, 9878–9887.
- [45] H. H. Johann, *Z. Phys. Chem.* **1931**, *69*, 185–206.
- [46] P. A. Malmqvist, B. O. Roos, B. Schimmelpfennig, *Chem. Phys. Lett.* **2002**, *357*, 230–240.
- [47] S. I. Bokarev, O. Kühn, *WIREs Comput. Mol. Sci.* **2020**, *10*, e1433.
- [48] B. O. Roos, R. Lindh, V. Veryazov, P.-O. Widmark, *J. Phys. Chem. A* **2004**, *108*, 2851–2858.
- [49] B. O. Roos, R. Lindh, V. Veryazov, P.-O. Widmark, *J. Phys. Chem. A* **2005**, *109*, 6575–6579.
- [50] S. I. Bokarev, M. Khan, M. K. Abdel-Latif, J. Xiao, R. Hilal, S. G. Aziz, E. F. Aziz, O. Kühn, *J. Phys. Chem. C* **2015**, *119*, 19192–19200.
- [51] O. S. Bokareva, G. Grell, S. I. Bokarev, O. Kühn, *J. Chem. Theory Comput.* **2015**, *11*, 1700–1709.
- [52] M. O. Krause, J. H. Oliver, *J. Phys. Chem. Ref. Data* **1979**, *8*, 329–338.
- [53] B. Valeur, *Molecular Fluorescence: Principles and Applications* **2001**.

Manuscript received: October 8, 2020
Revised manuscript received: December 21, 2020
Accepted manuscript online: January 7, 2021
Version of record online: March 16, 2021